

Sandwich spatial saturation for neuromelanin-sensitive MRI: Development and multi-center trial

Sooyeon Ji^a, Eun-Jung Choi^a, Beomseok Sohn^b, Kyoungwon Baik^b, Na-Young Shin^c,
Won-Jin Moon^d, Seongbeom Park^e, Soohwa Song^e, Phil Hyu Lee^f, Dong Hoon Shin^e,
Se-Hong Oh^g, Eung Yeop Kim^{h,*}, Jongho Lee^{a,*}

^a Laboratory for Imaging Science and Technology, Department of Electrical and Computer Engineering, Seoul National University, Seoul, Republic of Korea

^b Department of Radiology, Severance Hospital, Seoul, Republic of Korea

^c Department of Radiology, Catholic University of Korea, Seoul, Republic of Korea

^d Department of Radiology, Konkuk University Medical Center, Seoul, Republic of Korea

^e Heuron Co., Ltd., Republic of Korea

^f Department of Neurology, Severance Hospital, Seoul, Republic of Korea

^g Division of Biomedical Engineering, Hankuk University of Foreign Studies, Gyeonggi-do, Republic of Korea

^h Department of Radiology, Samsung Medical Center, Sungkyunkwan University College of Medicine, Seoul, Republic of Korea

ABSTRACT

Neuromelanin (NM)-sensitive MRI using a magnetization transfer (MT)-prepared T1-weighted sequence has been suggested as a tool to visualize NM contents in the brain. In this study, a new NM-sensitive imaging method, sandwichNM, is proposed by utilizing the incidental MT effects of spatial saturation RF pulses in order to generate consistent high-quality NM images using product sequences. The spatial saturation pulses are located both superior and inferior to the imaging volume, increasing MT weighting while avoiding asymmetric MT effects. When the parameters of the spatial saturation were optimized, sandwichNM reported a higher NM contrast ratio than those of conventional NM-sensitive imaging methods with matched parameters for comparability with sandwichNM (SandwichNM: $23.6 \pm 5.4\%$; MT-prepared TSE: $20.6 \pm 7.4\%$; MT-prepared GRE: $17.4 \pm 6.0\%$). In a multi-vendor experiment, the sandwichNM images displayed higher means and lower standard deviations of the NM contrast ratio across subjects in all three vendors (SandwichNM vs. MT-prepared GRE; Vendor A: $28.4 \pm 1.5\%$ vs. $24.4 \pm 2.8\%$; Vendor B: $27.2 \pm 1.0\%$ vs. $13.3 \pm 1.3\%$; Vendor C: $27.3 \pm 0.7\%$ vs. $20.1 \pm 0.9\%$). For each subject, the standard deviations of the NM contrast ratio across the vendors were substantially lower in SandwichNM (SandwichNM vs. MT-prepared GRE; subject 1: 1.5% vs. 8.1% , subject 2: 1.1% vs. 5.1% , subject 3: 0.9% vs. 4.0% , subject 4: 1.1% vs. 5.3%), demonstrating consistent contrasts across the vendors. The proposed method utilizes product sequences, requiring no alteration of a sequence and, therefore, may have a wide practical utility in exploring the NM imaging.

1. Introduction

Neuromelanin (NM) is a dark insoluble pigment found abundantly in catecholaminergic cells of substantia nigra pars compacta (SNc) and locus coeruleus (LC), and the pigment is known to accumulate during normal aging (Fedorow et al., 2005; Zecca et al., 2004). NM abnormality has long been associated with Parkinson's disease (PD) because of the selective death of NM containing cells in PD patients (Greenfield and Bosanquet, 1953), which results in a visible loss of the pigment in SNc and LC (Halliday et al., 2014; Kastner et al., 1992).

NM-sensitive MRI or NM-MRI (Sasaki et al., 2006; Chen et al., 2014; Cassidy et al., 2019) is a non-invasive proxy measure of NM in the human brain, which may provide valuable information about PD (Huddleston et al., 2018, 2017; Ohtsuka et al., 2013; Sulzer et al., 2018) and other neurological disorders (Matsuura et al., 2013; Miyoshi et al., 2013; Moon et al., 2016; Pyatigorskaya et al., 2017; Shibata et al., 2008). In particular, NM-MRI has displayed the ability to discriminate between healthy control and PD patients (Reimão et al., 2015; Schwarz et al.,

2017), and between PD and other neurological diseases such as idiopathic PD and Alzheimer's disease (Miyoshi et al., 2013; Moon et al., 2016; Pyatigorskaya et al., 2018). It has also shown correlation with PD progression (Fabbri et al., 2017; Gaurav et al., 2021; Schwarz et al., 2017, 2011; Xing et al., 2022), revealing its potential as a biomarker of PD.

To generate NM-sensitive MRI images, magnetization transfer (MT) imaging with T1-weighting is commonly used (Cassidy et al., 2019; Langley et al., 2017; Liu et al., 2020; Schwarz et al., 2011). This combination of the contrasts can be explained as follows: For T1-weighting, NM exists in the form of a paramagnetic NM-iron complex, which leads to a shortened T1 of NM containing voxels (Sulzer et al., 2018). For MT, the NM-abundant tissues, which have relatively low macromolecular content due to the large dopamine cell bodies, are surrounded by a tissue with high macromolecular content (e.g., crus cerebri or CC), which leads to a suppressed signal when MT pulses are applied. Therefore, MT imaging with T1-weighting highlights T1-shortened NM-containing voxels while suppressing the surrounding tissues (Cassidy et al., 2019;

* Corresponding authors.

E-mail addresses: eungyeop.kim@gmail.com (E.Y. Kim), jonghoyi@snu.ac.kr (J. Lee).

<https://doi.org/10.1016/j.neuroimage.2022.119706>.

Received 23 August 2022; Received in revised form 9 October 2022; Accepted 20 October 2022

Available online 28 October 2022.

1053-8119/© 2022 The Authors. Published by Elsevier Inc. This is an open access article under the CC BY-NC-ND license

(<http://creativecommons.org/licenses/by-nc-nd/4.0/>)

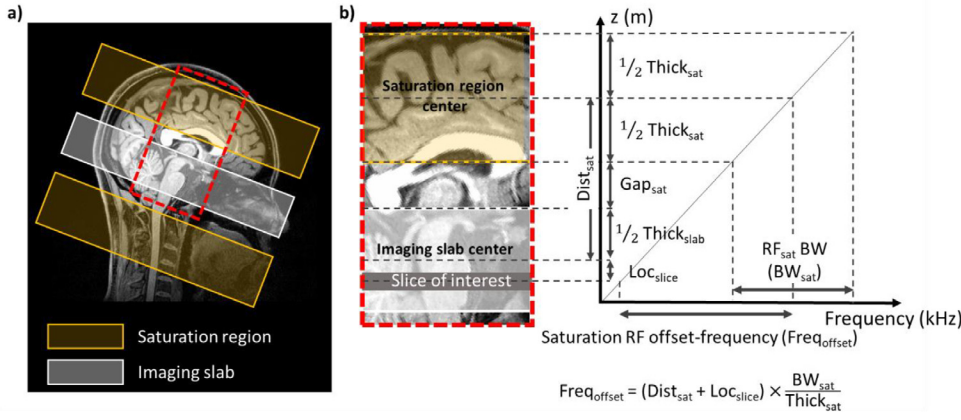


Fig. 1. (a) Illustration of sandwichNM imaging and (b) offset-frequency of a single spatial saturation pulse. SandwichNM imaging uses spatial saturation pulses for magnetization transfer (MT) weighting; an even number of saturation pulses are alternately applied inferior and superior to the imaging volume for symmetric MT effects across slices. The offset-frequency of the saturation RF ($\text{Freq}_{\text{offset}}$) is determined as shown in the equation (Eq. (1)). In sandwichNM imaging, this position dependent offset-frequency, which leads to a position dependent MT effect, is compensated by the same RF pulse at the opposite side of the imaging slab, generating position independent MT-weighting.

Oshima et al., 2020; Trujillo et al., 2017). So far, several MT-prepared TSE and GRE protocols have been proposed, delineating NM (Cassidy et al., 2019; Langley et al., 2017; Liu et al., 2020).

While the option of applying an MT pulse is available in all vendors, it is well-known that the MT pulse parameters such as pulse shape, flip angle, duration, and offset frequency, which govern saturation efficiency, are often fixed in product sequences and substantially differ across vendors and sequences. For example, a previous study reported a difference between the Siemens and Philips off-resonance MT pulses (e.g., flip angle of 500° and 220° for Siemens and Philips, respectively) and the resulting inter-site bias between semi-quantitative MT maps (Leutritz et al., 2020). Furthermore, the mechanism of the MT saturation may also differ by vendor or sequence (e.g., off-resonance vs. on-resonance). These MT parameter differences between vendors limit direct comparisons between images. An alternative option is to develop a custom-designed MT sequence for all vendors, but this requires substantial efforts for programming sequences for each software version and upgrade, making this solution less attractive for clinical use.

In this study, we propose a new NM imaging method, sandwichNM, which uses the incidental MT effects of spatial saturation pulses for MT-weighting (Ji et al., 2021). The spatial saturation pulse, which is available in the product sequences of all vendors, is controllable because the amount of MT effects can be modified by the number of pulses deployed and the offset-frequency can be changed by the location and thickness of the pulses, giving freedom and usability with no effort for sequence programming. In sandwichNM, the saturation bands are placed both inferior and superior to the imaging volume, like a sandwich, balancing MT weighting across slices (Fig. 1). Here, we assess and optimize the effects of the sandwich saturation pulses on the NM contrast using computer simulations and *in-vivo* experiments. Then, *in-vivo* images are compared with those of conventional MT-prepared 3D GRE (MT-GRE) and 2D TSE (MT-TSE) methods using a vendor-supplied MT pulse. Finally, multi-vendor experiments are conducted to emphasize the effectiveness and usability of sandwichNM imaging.

2. Theory

2.1. Position dependent MT effects of a spatial saturation pulse

In this section, we analyze the position dependent MT effects of a spatial saturation pulse. A schematic drawing of the proposed method and

the slice location-dependent offset-frequency of a spatial saturation RF pulse are depicted in Fig. 1. The spatial saturation pulse is applied with a slice selection gradient. Therefore, the offset-frequency ($\text{Freq}_{\text{offset}}$) is defined as follows:

$$\text{Freq}_{\text{offset}} = (\text{Dist}_{\text{sat}} + \text{Loc}_{\text{slice}}) \times \frac{\text{BW}_{\text{sat}}}{\text{Thick}_{\text{sat}}} \quad (1)$$

where Dist_{sat} is the center-to-center distance between the saturation region and the imaging slab, $\text{Loc}_{\text{slice}}$ is the location of the slice of interest with respect to the center of the imaging slab, BW_{sat} is the bandwidth of the saturation RF pulse, and $\text{Thick}_{\text{sat}}$ is the thickness of the spatial saturation. Dist_{sat} is determined by $\text{Thick}_{\text{sat}}$, the saturation gap (Gap_{sat}), and the imaging slab thickness ($\text{Thick}_{\text{slab}}$) as follows:

$$\text{Dist}_{\text{sat}} = 0.5\text{Thick}_{\text{sat}} + \text{Gap}_{\text{sat}} + 0.5\text{Thick}_{\text{slab}} \quad (2)$$

Combining the two equations, the offset-frequency is proportional to Gap_{sat} and inversely proportional to $\text{Thick}_{\text{sat}}$ for fixed $\text{Thick}_{\text{slab}}$ and BW_{sat} . Therefore, using a smaller Gap_{sat} and larger $\text{Thick}_{\text{sat}}$ would increase MT saturation. However, this would inevitably increase the amount of direct saturation (Graham and Henkelman, 1997) and decrease the image signal to noise ratio (SNR).

As shown in Eq. (1), the offset-frequency is related to $\text{Loc}_{\text{slice}}$. This implies that the application of single-sided spatial saturation results in asymmetric MT effects across slices. To avoid this asymmetry, we propose to apply spatial saturation pulses both inferior and superior to the imaging slab with the same distance from the imaging volume (Fig. 1a). Hence, an even number of flow saturation pulses (e.g., 2, 4, 6) are applied, with a pair of pulses applied superior and inferior to the imaging volume. This application of spatial saturation is hereafter referred to as sandwich saturation.

3. Materials and methods

3.1. Simulation of MT effects of spatial saturation pulses

To assess the effect of spatial saturation pulses on the image contrast, the signal intensity of SNc and a reference region (CC) at the slice position ($\text{Loc}_{\text{slice}}$) was simulated numerically by solving the Bloch equation for free water and macromolecular populations (Graham and Henkelman, 1997):

$$\frac{d\mathbf{M}}{dt} = \begin{bmatrix} -R_2^f & -\text{Freq}_{\text{offset}}(\text{Loc}_{\text{slice}}) & 0 & 0 \\ -\text{Freq}_{\text{offset}}(\text{Loc}_{\text{slice}}) & -R_2^f & -\omega_1(t) & 0 \\ 0 & \omega_1(t) & -(R_1^f + k_{fm}) & k_{mf} \\ 0 & 0 & 0 & -(R_1^m + k_{mf} + W(t)) \end{bmatrix} \begin{bmatrix} M_x^f \\ M_y^f \\ M_z^f \\ M_z^m \end{bmatrix} + \begin{bmatrix} 0 \\ 0 \\ R_1^f M_0^f \\ R_1^m M_0^m \end{bmatrix} \quad (3)$$

Table 1

Sequence parameters for the multi-vendor study. Both $N_{\text{sat}} = 2$ with TR = 30 ms and $N_{\text{sat}} = 4$ with TR = 60 ms sandwichNM images were acquired and compared with the images of MT-GRE of the same parameters. All sequences were the product sequences of the vendors with no modification.

Vendor	Base sequence	N_{sat}	TR [ms]	FA [°]	TE [ms]	resolution [mm ³]	Acq. matrix size	TA	Num. of averages	Sandwich saturation parameters	Note
Philips	3D FFE	2	30	14	4	$0.8 \times 0.8 \times 1.2$	$320 \times 220 \times 32$	5:30	2	Thick _{sat} = 80 mm Gap _{sat} = 10 mm	Elliptical scanning
		4	60	20	3.62	$0.8 \times 0.8 \times 1.2$	$320 \times 220 \times 32$	5:34	1	Thick _{sat} = 80 mm Gap _{sat} = 10 mm	Elliptical scanning
GE	3D Vasc TOF	2	30	14	2	$0.8 \times 0.8 \times 1.2$	$320 \times 182 \times 32$	5:49	2	Thick _{sat} = 80 mm Gap _{sat} = 10 mm	Slice oversampling Reduced FOV
		4	60	20	2	$0.8 \times 0.8 \times 1.2$	$320 \times 182 \times 32$	5:49	1	Thick _{sat} = 80 mm Gap _{sat} = 10 mm	Slice oversampling Reduced FOV
Siemens	3D GRE	2	30	14	3.62	$0.8 \times 0.8 \times 1.2$	$320 \times 220 \times 32$	5:34	2	Thick _{sat} = 80 mm Gap _{sat} = 10 mm	Elliptical scanning
		4	60	20	3.62	$0.8 \times 0.8 \times 1.2$	$320 \times 220 \times 32$	5:34	1	Thick _{sat} = 80 mm Gap _{sat} = 10 mm	Elliptical scanning

where superscript f (or m) denotes the free water (or macromolecular) pool, respectively, $R_{1 \text{ (or 2)}}$ denotes the relaxation rates, $k_{\text{fm (or mf)}}$ is the exchange rate from free to macromolecular (or macromolecular to free) pool, $M_x \text{ (or y or z)}$ is the x (or y, or z) magnetization, M_0 is the initial magnetization, $\omega_1(t)$ is the time-varying amplitude of the flow saturation pulse, and $W(t) = \pi \omega_1^2(t) g(\Delta(dS), R_2^m)$ is the saturation rate of the macromolecular pool. The line shape of the macromolecular pool, $g(\Delta(dS), R_2^m)$, was chosen to be super-Lorentzian (Morrison and Henkelman, 1995). The simulation parameters for SNc and CC were summarized in Supplementary Table 1, which were adapted from a previous study (Trujillo et al., 2019). M_0^f of SNc and CC are set to be 1 and 0.86, respectively (see Supplementary Fig. 1 for details).

The parameters of RF pulses were matched to those in the experiments using Siemens 3T MRI (Trio, Siemens, Erlangen, Germany). The duration of the spatial saturation pulse and the excitation pulse for the simulation were 3.84 ms and 1 ms, respectively. The flip angle (FA) of the spatial saturation pulse was set to 90° and the time bandwidth product was 8.33, resulting in an RF bandwidth of 2.17 kHz. There was a 3 ms gap between consecutive spatial saturation pulses despite the gap between the last spatial saturation pulse and the excitation pulse having been set to 1.97 ms. The imaging slab thickness was 40 mm, and the signals of SNc and CC were simulated using 1600 spins uniformly distributed throughout the slab. The imaging slab was divided into 16 slices; the SNc and CC signals of 100 spins located in each slice were averaged. Finally, the contrast ratio (CR) between SNc and CC was calculated for each slice (Sasaki et al., 2006):

$$CR(\%) = \frac{(I_{\text{SN}} - I_{\text{CC}})}{I_{\text{CC}}} \times 100, \quad (4)$$

where I_{SN} and I_{CC} are the signals of SNc and CC, respectively.

Several conditions and parameters were tested with the default parameters of $N_{\text{sat}} = 4$, Gap_{sat} = 10 mm, and Thick_{sat} = 80 mm. First, the sandwich saturation scheme was compared to the single-sided saturation scheme in order to assess the uniformity of the MT effects across the imaging slab. Then, the effects of Gap_{sat} and Thick_{sat} were assessed by changing Gap_{sat} from 0 to 100 mm with a 10 mm interval, and Thick_{sat} from 20 to 110 mm with a 10 mm interval. The number of spatial saturations (N_{sat}) was also tested for 2 and 4. For N_{sat} of 4, TR was 60 ms and FA was 20° (TR and FA adapted from Liu et al. (2020)). For N_{sat} of 2, TR and FA were adjusted to 30 ms and 14°, respectively.

3.2. MRI experiments

Three experiments, one to determine the spatial saturation parameters, another to compare sandwichNM with conventional NM methods, and the third to evaluate multi-vendor performances, were conducted. The study was approved by IRB and a total of eight subject, who provided written consent, were scanned (three for the first experiment, one for the second experiment, and four for the last experiment). In the first two experiments, data were collected using 3T MRI from Siemens (Trio, Siemens, Erlangen, Germany), whereas in the multi-vendor experiment, scans were performed using 3T MRI systems from three dif-

ferent vendors (Skyra, Siemens, Erlangen, Germany; Ingenia CX, Philips, Best, Netherlands; Discovery750, GE, Milwaukee, WI) in three different MRI centers (Samsung Medical Center, Seoul, Korea; Severance Hospital, Seoul, Korea; Konkuk University Hospital, Seoul, Korea).

[Optimization for spatial saturation parameters] The default sequence parameters for sandwichNM were as follows: FOV = $230 \times 230 \times 40$ mm³, voxel size = $0.5 \times 0.5 \times 2.5$ mm³, TR/TE = 60/3.86 ms, FA = 20°, readout bandwidth = 170 Hz/pixel, $N_{\text{sat}} = 4$, Gap_{sat} = 10 mm, Thick_{sat} = 80 mm, and acquisition time = 5 min 30 s. The imaging slab was oriented perpendicular to the 4th ventricle, and the center of the imaging volume was located tangent to the top of the pons.

To compare the results with those of the computer simulation and also to determine the sequence parameters that provide the best NM contrast, four tests were conducted. First, to evaluate the uniformity of the MT effects, the sandwich saturation scheme and the single-sided saturation scheme were acquired and compared (one subject). Then, to measure the effects of Gap_{sat}, the sandwichNM acquisition was repeated with Gap_{sat} = 0, 10, 50, and 100 mm (one subject). After that, the effects of Thick_{sat} were assessed by changing Thick_{sat} (20, 50, 80, and 110 mm; one subject). Finally, the two different settings of N_{sat} , one with $N_{\text{sat}} = 2$, TR = 30 ms, and FA = 14°, and the other with $N_{\text{sat}} = 4$, TR = 60 ms, and FA = 20°, were compared. The last experiment was conducted using the data of the multi-vendor experiment (see **multi-vendor experiment**).

For each experiment, regions of interest (ROIs) were manually drawn for SNc and CC using MATLAB (Mathworks Inc., Natick, MA), and CR between the mean signal intensities of SNc and CC was calculated. The SNR of SNc was also calculated to account for the signal drop resulting from the MT effects.

[Comparison with conventional NM imaging methods] Two conventional NM-sensitive images, MT-GRE and MT-TSE, were acquired, and the results were compared with that of the sandwichNM. The parameters for the MT pulse were offset-frequency = 1200 Hz, FA = 500°, and RF bandwidth = 230 Hz. The 3D GRE sequence parameters were matched to the sandwichNM parameters, while 2D TSE images were acquired with FOV = 230×230 mm², slice thickness = 2.5 mm, voxel size = 0.5×0.5 mm², TR = 910 ms, TE = 14 ms, turbo factor = 6, concatenation = 2, number of averages = 2, readout bandwidth = 120 Hz/pixel, and acquisition time = 4 min 36 s (adapted from Pyatigorskaya et al. (2020)). The SNR and CR were calculated for all three methods in three slices containing the largest SNc volume.

[Multi-vendor experiment] At each scanner, sandwichNM and MT-GRE images were acquired using product sequences with no modification. The scan protocol parameters are summarized in Table 1. The protocols with $N_{\text{sat}} = 2$ and 4 were both acquired for comparison. Note that a different FOV was used for the GE scanner because there was no option available for elliptical scanning or slice oversampling.

For analysis, the sandwichNM and MT-GRE images that were acquired using the Siemens and GE scanners were rigidly registered to the sandwichNM image acquired from the Philips scanner using the FMRIB's Linear Image Registration Tool (FSL FLIRT) (Jenkinson et al., 2012). The ROIs of SNc and CC were drawn on the sandwichNM images acquired

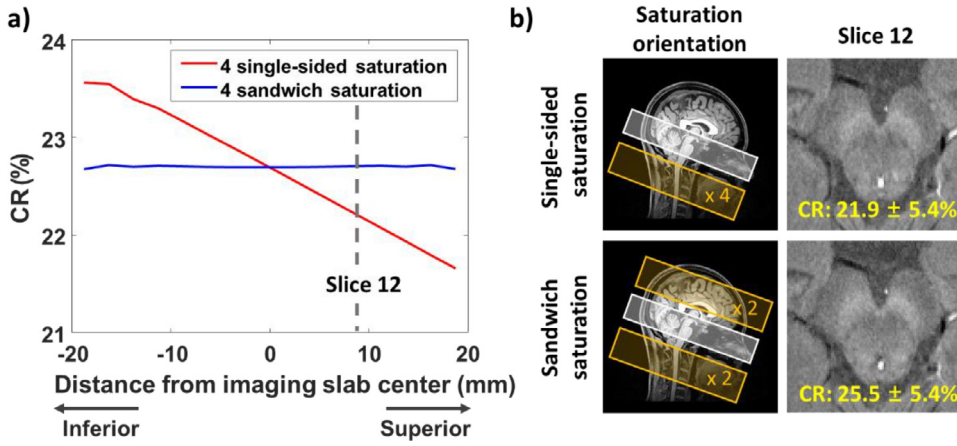


Fig. 2. (a) Simulation results and (b) experimental results of the single-sided scheme and the sandwich saturation scheme. When the spatial saturation pulses are applied inferior to the imaging slab, CR decreases toward the superior end of the imaging slab (red line). On the other hand, the sandwich saturation scheme shows a flat CR across the imaging slab (blue line). In the experiment, the slice above the center of the slab (slice 12) reports a lower CR ($21.9 \pm 5.4\%$) in the single-sided scheme than that ($25.5 \pm 5.4\%$) in the sandwich saturation scheme.

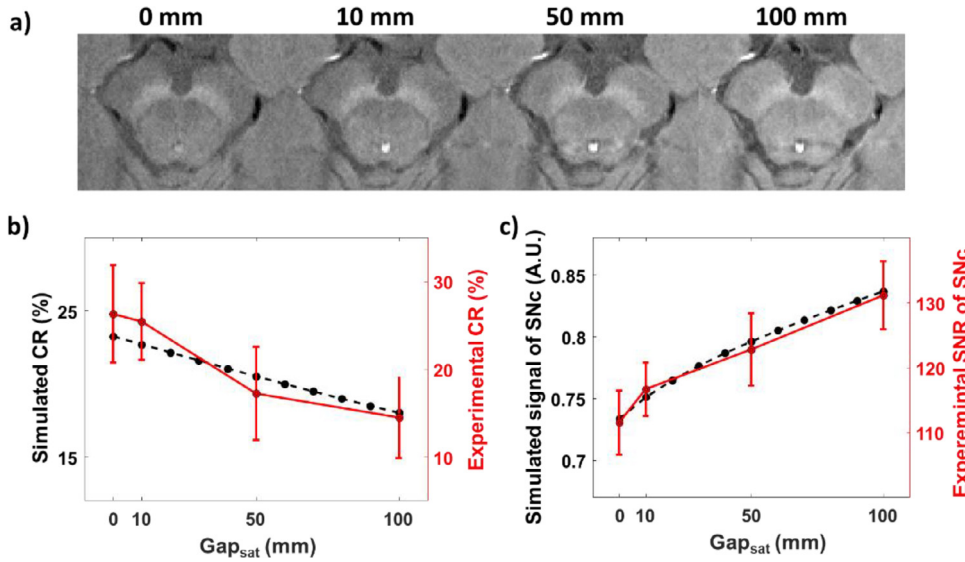


Fig. 3. (a) Images with Gap_{sat} = 0, 10, 50, and 100 mm displayed for a representative slice. (b) CRs and (c) signal intensities and SNRs plotted over Gap_{sat}. The simulation results are displayed in black dashed lines while the experimental results are displayed in red solid lines. Error bars indicate standard deviations. Both simulated and experimental CRs decrease with Gap_{sat} whereas both simulated signal intensity and experimental SNRs increase with Gap_{sat}.

from the Philips scanner. Then the CR between SNc and CC were calculated as defined in Eq. (4).

4. Results

The simulation results of the sandwich saturation scheme and the single-sided saturation scheme are displayed in Fig. 2a. In the single-sided scheme, CR predominantly decreases towards the superior slices due to the asymmetric MT effects of the spatial saturation pulses (Fig. 2a: red line). In the sandwich saturation scheme, however, CR is almost uniform across the slices, demonstrating the advantage of the approach (Fig. 2a: blue line). The simulation results are partially supported by the experimental results shown in Fig. 2b where CR in a relatively superior slice (slice 12) is higher in the sandwich saturation ($25.5 \pm 5.4\%$) than in the single-sided saturation ($21.9 \pm 5.4\%$), agreeing with the simulation results.

When the CR and signal intensity of SNc are simulated for various Gap_{sat}, CR decreases and signal intensity increases as Gap_{sat} increases (Fig. 3b, c; black dashed lines). These results are in agreements with the experimental results of CR and SNR (Fig. 3b, c; red solid lines).

When the CR and signal intensity of SNc are simulated for various Thick_{sat}, CR increases and signal intensity decreases as Thick_{sat} increases (Fig. 4b, c; black dashed lines), supporting the experimental results (Fig. 4b, c; red solid lines).

The simulated CR of N_{sat} = 2 is 22.7 %, and is comparable to that of N_{sat} = 4 (22.4 %). These comparable CR values are confirmed by

the experiments ($28.1 \pm 6.7\%$ when N_{sat} = 2 vs. $27.2 \pm 5.7\%$ when N_{sat} = 4; Fig. 5 and Supplementary Table 2). Additionally, SNRs of SN using the two parameters are also similar (224 ± 12 when N_{sat} = 2 vs. 249 ± 11 when N_{sat} = 4). Because setting two saturation bands is more convenient during scanning, the final parameters for sandwichNM are N_{sat} = 2, TR = 30 ms, FA = 14°, Gap_{sat} = 10 mm, and Thick_{sat} = 80 mm where the last two parameters are chosen to balance between SNR and CR.

When this sandwichNM acquisition is compared with the conventional methods, the results show the highest CR in the sandwichNM images ($23.6 \pm 5.4\%$) followed by MT-TSE ($20.6 \pm 7.4\%$) and MT-GRE ($17.4 \pm 6.0\%$) (Fig. 6). The SNR of sandwichNM (121 ± 5) is slightly lower than that of MT-GRE (135 ± 7), but higher than that of MT-TSE (98 ± 6). The results were consistent when ROIs were drawn on the images from the conventional sequences (Supplementary Table 3). Furthermore, the MT-GRE images suffer from flow artifacts whereas the proposed method does not because of the saturation bands. Hence, the overall results of sandwichNM are superior to those of the conventional methods.

The results of the multi-vendor study are displayed in Fig. 7 (results of N_{sat} = 4 summarized in Supplementary Fig. 2). The sandwichNM images provide high and consistent contrasts across the scanners (Fig. 7a) while the MT-GRE images suffer from flow artifacts and contrast variations (Fig. 7b). The mean CRs of the sandwichNM images across all subjects are higher than those of MT-GRE images in all three vendors (Fig. 7c: $28.4 \pm 1.5\%$ vs. $24.4 \pm 2.8\%$, $27.2 \pm 1.0\%$ vs. $13.3 \pm 1.3\%$, and

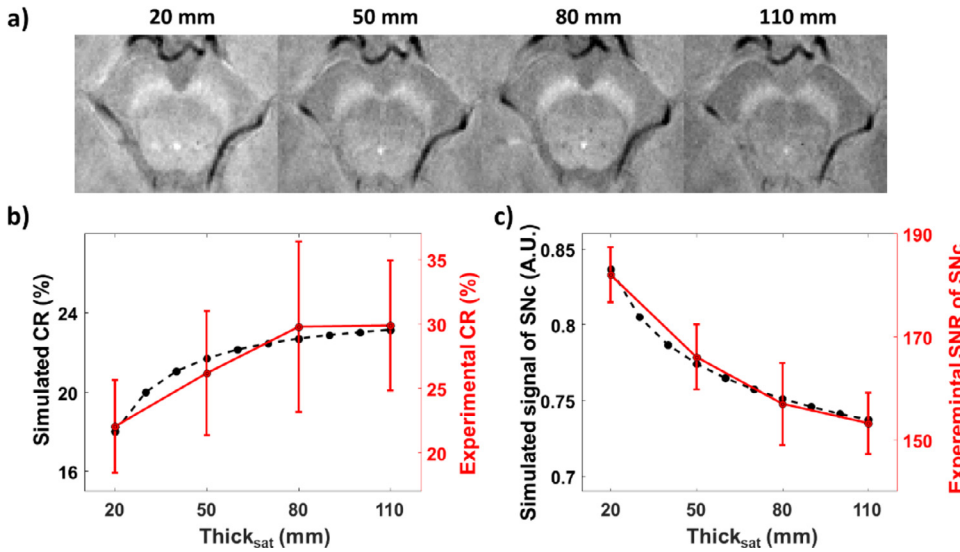


Fig. 4. (a) Images with Thick_{sat} = 20, 50, 80, and 110 mm displayed for a representative slice. (b) CRs and (c) signal intensities and SNRs plotted over Thick_{sat}. The simulation results are displayed in black dashed lines while the experimental results are displayed in red solid lines. Error bars indicate standard deviations. Both simulated and experimental CRs increase with Thick_{sat}, whereas both simulated signal intensity and experimental SNRs decrease with Thick_{sat}.

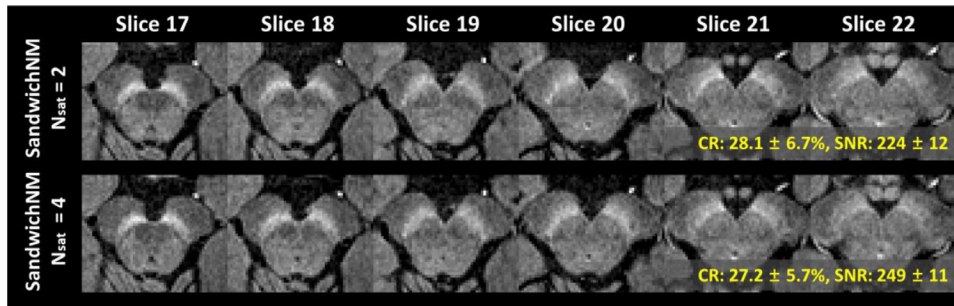


Fig. 5. Comparison between sandwichNM results acquired using N_{sat} = 2 with TR = 30 ms vs. N_{sat} = 4 with TR = 60 ms. Both parameters report comparable CRs ($28.1 \pm 6.7\%$ when N_{sat} = 2 vs. $27.2 \pm 5.7\%$ when N_{sat} = 4) and SNRs (224 ± 12 when N_{sat} = 2 vs. 249 ± 11 when N_{sat} = 4).

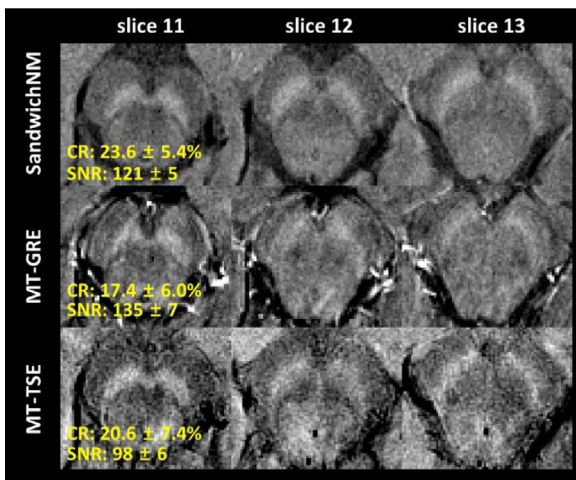


Fig. 6. Comparison between sandwichNM and conventional NM methods. SandwichNM images display the highest CR ($23.6 \pm 5.4\%$), followed by those of MT-TSE ($20.6 \pm 7.4\%$) and MT-GRE ($17.4 \pm 6.0\%$). While the SNR of the sandwichNM images (121 ± 5) is slightly lower than that of MT-GRE (135 ± 7) but it is higher than that of MT-TSE (98 ± 6).

$27.3 \pm 0.7\%$ vs. $20.1 \pm 0.9\%$ for Philips, GE, and Siemens, respectively). When the mean CRs are calculated for each subject across vendors, the sandwichNM images display higher means and lower standard deviations compared to those of the MT-GRE images (Fig. 7c: $28.6 \pm 1.5\%$ vs. $20.1 \pm 8.1\%$, $27.1 \pm 1.1\%$ vs. $19.4 \pm 5.1\%$, $27.6 \pm 0.9\%$ vs. $18.0 \pm 4.0\%$, and $27.2 \pm 1.1\%$ vs. $19.5 \pm 5.3\%$, for subjects 1, 2, 3, and 4,

respectively). These lower standard deviations suggest lower variability across vendors.

5. Discussion

In this study, we proposed a new NM imaging method, sandwichNM, which provides consistent and high-quality images across scanners from different vendors.

The computer simulated CR values deviated from the experimental CR values (simulated CR: 22.7% vs. experimental CR: $27.3 \pm 0.7\%$ for the default parameters using N_{sat} = 2). This difference may be explained by the sensitivity of CR to the tissue parameters, particularly the pool size ratio. In our simulation, the parameters were adopted from Trujillo et al. (2019). When the simulation was repeated with another parameters within one standard deviations from the mean values of the pool size ratio, CR became 28.7% , revealing a better agreement with the experimental value.

In this study, we suggested two protocols of sandwichNM imaging: N_{sat} = 2 with TR = 30 ms and N_{sat} = 4 with TR = 60 ms, both of which demonstrated comparable CRs and SNRs (Fig. 5, Supplementary Table 2). Practically, applying the two saturation bands (i.e., N_{sat} = 2) is preferable in a clinical setting because the majority of MRI scanners provide options to automatically apply two parallel saturation bands superior and inferior to the imaging volume. Hence, the protocol setting during scanning is easier and can be consistent in all subjects. The consistent positioning of the saturation bands is important because it influences the NM contrast (Figs. 3 and 4). On the other hand, the N_{sat} = 4 setting can acquire four to five echo data with no cost in acquisition time. These multi-echo data may be utilized for susceptibility-based nigral hyperintensity imaging (Kim et al., 2019; Nam et al., 2017). Alternatively, one may increase N_{sat} from 4 to 6 in the case of TR = 60 ms,

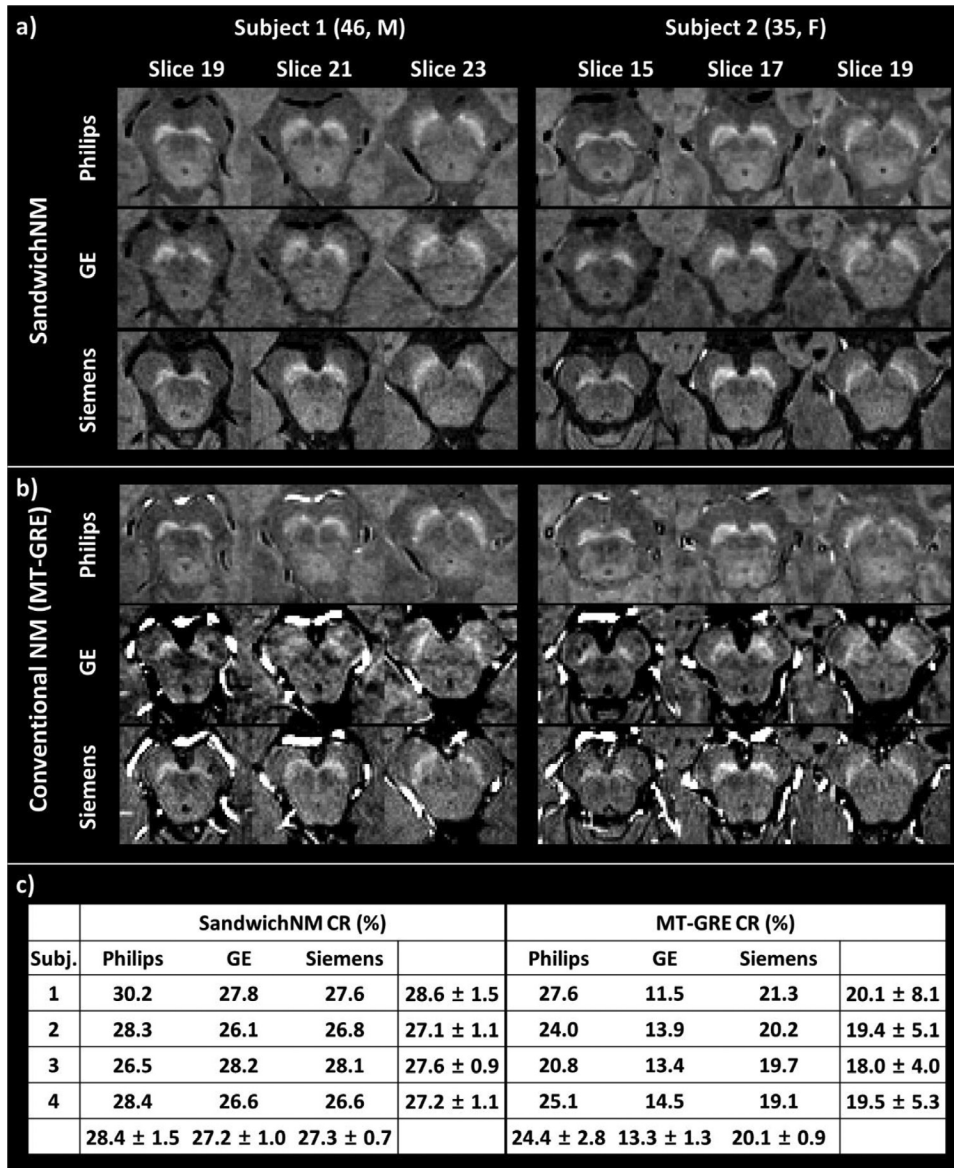


Fig. 7. Multi-vendor study results of (a) sandwichNM ($N_{\text{sat}} = 2$) vs. (b) MT-GRE NM, displaying images from two subjects. When averaged across all four subjects, the sandwichNM results report higher CR values and lower standard deviations than those of conventional NM in all three vendors. Furthermore, when the mean CRs are calculated for each subject across vendors, the sandwichNM images yield higher means and lower standard deviations compared to those of the MT-GRE images, suggesting lower variability across vendors.

further increasing MT weighting. But this change may decrease SNR and induce a higher specific absorption rate (SAR), hitting the SAR limit. In our experiments, SandwichNM was tested for two different resolutions: one with a high in-plane resolution ($0.5 \times 0.5 \text{ mm}^2$) and a thick slice (2.5 mm); and the other with a moderate in-plane resolution ($0.8 \times 0.8 \text{ mm}^2$) and a thin slice (1.2 mm). These options resulted in differences in image quality and SNR (Figs. 5 vs. 6). They may have different applications. For instance, the protocol using the high in-plane resolution may better visualize LC, which is known to have a thin cylindrical structure of 2–2.5 mm thickness (Fernandes et al., 2012) (Supplementary Fig. 3). Our imaging volume is large enough to cover both SN and LC when it is appropriately located. In this study, however, we focused on optimizing the method for the SN structure, and therefore the performance of sandwichNM on LC imaging is the subject of a future study.

The sandwichNM CR values reported in our parameter optimization experiments were somewhat different from those in the multi-vendor experiments (e.g., 23.6% in Fig. 6 vs. 28.1% in subject 3 of Fig. 7c). This difference may be explained by the well-known age effects of the NM contrast (age of 24 for the subject in Fig. 6 vs. age of 30 for the subject 3 in Fig. 7c) (Xing et al., 2018).

SandwichNM displayed relatively consistent contrasts across scanners. However, we must note that TE was different from one vendor to another (4, 2, and 3.62 ms for Philips, GE, and Siemens, respectively). This difference may have influenced the NM contrasts because the iron in SN may induce different T_2^* decays for different TEs although the effects can be limited due to the short TEs. Additionally, the saturation pulse type or shape applied in each vendor or each software or hardware version of scanners was not considered. For example, the saturation pulse parameters of Siemens had duration = 3.84 ms and bandwidth = 2.18 kHz while those of GE had duration = 4 ms and bandwidth = 1.23 kHz. Despite these differences, our multi-vendor study results suggest that sandwichNM reports much more consistent outcomes than those of the conventional NM results, suggesting the advantage of the method.

Despite the correlation between NM concentration and MRI NM contrast (Cassidy et al., 2019), the later is expected to have contributions from other factors (e.g., myelin concentration in surrounding white matter). Furthermore, the portion of NM and non-NM factors is not well studied and may vary among acquisition methods. Therefore, one has to be cautious in interpreting the contrast and also exploration for NM specificity is necessary.

The scan time and voxel size of the conventional NM-MRI methods were matched to those of sandwichNM for fair comparison between methods. Therefore, the sequence parameters such as voxel size or number of averages are different from previously published methods. For example, in a study by Pyatigorskaya et al. (2020), TSE was acquired with the voxel size of $0.4 \times 0.4 \times 3 \text{ mm}^3$ and three averages. This would result in a higher SNR at the cost of a longer scan time. Another study proposed to use a 2D MT-GRE sequence with a customized MT pulse (Wengler et al., 2020), showing high quality SN images. But the approach was not compared with our method because it requires a customized sequence.

Manually drawn ROIs were utilized for CR and SNR calculation in this study. Using automated methods such as deep-learning based segmentation (Kang et al., 2021; Tessema et al., 2022) or atlas-based ROIs (Pauli et al., 2018) may enhance anatomical targeting.

The large deviations of the MT-GRE results may originate from the MT pulse differences across vendors. The Philips MT-GRE images, which utilized an on-resonance MT pulse, reported larger CRs ($24.4 \pm 2.8\%$) than those from GE and Siemens, which utilized off-resonance MT pulses ($13.3 \pm 1.3\%$ for GE and $20.1 \pm 0.9\%$ for Siemens). Furthermore, although vendor-supplied MT pulses from Siemens and GE both applied off-resonance pulses, parameters such as pulse shape, duration, FA, and offset frequency were substantially different (Siemens: Gaussian pulse, 10 ms, 500° , 1.2 kHz; GE: Fermi pulse, 8 ms, subject dependent variable, 2.4 kHz), resulting in significantly different MT effects.

6. Conclusion

The newly-proposed sandwichNM method provides a higher contrast between NM-containing tissue and surrounding area than the conventional NM methods. Moreover, the method produces a consistent contrast across multiple vendor scanners, facilitating the use of sandwichNM for multi-site studies. Because the method is based on product sequences, requiring no effort for sequence programming, we believe it has a wide applicability when exploring NM imaging.

Data and code availability

All data needed to evaluate the conclusions in the paper are present in the paper and/or the Supplementary Materials. Additional data and codes related to this paper can be obtained from the authors upon request (snu.list.software@gmail.com).

Data availability

Data will be made available on request.

Credit authorship contribution statement

Sooyeon Ji: Conceptualization, Methodology, Software, Writing – original draft, Writing – review & editing. **Eun-Jung Choi:** Formal analysis, Data curation, Writing – review & editing. **Beomseok Sohn:** Resources, Validation, Writing – review & editing. **Kyoungwon Baik:** Resources, Investigation, Writing – review & editing. **Na-Young Shin:** Resources, Investigation, Writing – review & editing. **Won-Jin Moon:** Resources, Validation, Writing – review & editing. **Seongbeom Park:** Investigation, Validation, Writing – review & editing. **Soohwa Song:** Investigation, Validation, Writing – review & editing. **Phil Hyu Lee:** Resources, Validation, Writing – review & editing. **Dong Hoon Shin:** Validation, Investigation, Writing – review & editing. **Se-Hong Oh:** Investigation, Writing – review & editing. **Eung Yeop Kim:** Validation, Supervision, Writing – review & editing. **Jongho Lee:** Supervision, Writing – review & editing.

Acknowledgement

This work was supported by Heuron Co., Ltd, National Research Foundation of Korea (NRF2021M3E5D2A01024795, NRF2021R1A2B5B03002783, and NRF 2022R1F1A1073551), Creative-Pioneering Researchers Program, INMC and IOER at Seoul National University.

Supplementary materials

Supplementary material associated with this article can be found, in the online version, at doi:10.1016/j.neuroimage.2022.119706.

References

- Cassidy, C.M., Zucca, F.A., Girgis, R.R., Baker, S.C., Weinstein, J.J., Sharp, M.E., Bellei, C., Valmadre, A., Vanegas, N., Kegeles, L.S., Brucato, G., Kang, U.J., Sulzer, D., Zecca, L., Abi-Dargham, A., Horga, G., 2019. Neuromelanin-sensitive MRI as a noninvasive proxy measure of dopamine function in the human brain. *Proc. Natl. Acad. Sci.* 116, 201807983. doi:10.1073/pnas.1807983116.
- Chen, X., Huddleston, D.E., Langley, J., Ahn, S., Barnum, C.J., Factor, S.A., Levey, A.I., Hu, X., 2014. Simultaneous imaging of locus coeruleus and substantia nigra with a quantitative neuromelanin MRI approach. *Magn. Reson. Imaging* 32, 1301–1306. doi:10.1016/j.mri.2014.07.003.
- Fabbri, M., Reimão, S., Carvalho, M., Nunes, R.G., Abreu, D., Guedes, L.C., Bouça, R., Lobo, P.P., Godinho, C., Coelho, M., Gonçalves, N.C., Rosa, M.M., Antonini, A., Ferreira, J.J., 2017. Substantia nigra neuromelanin as an imaging biomarker of disease progression in Parkinson's disease. *J. Park. Dis.* 7, 491–501. doi:10.3233/jpd-171135.
- Fedorow, H., Tribi, F., Halliday, G., Gerlach, M., Riederer, P., Double, K.L., 2005. Neuromelanin in human dopamine neurons: comparison with peripheral melanins and relevance to Parkinson's disease. *Prog. Neurobiol.* 75, 109–124. doi:10.1016/j.pneurobio.2005.02.001.
- Fernandes, P., Regala, J., Correia, F., Gonçalves-Ferreira, A.J., 2012. The human locus coeruleus 3-D stereotactic anatomy. *Surg. Radiol. Anat.* 34, 879–885. doi:10.1007/s00276-012-0979-y.
- Gaurav, R., Yahia-Cherif, L., Pyatigorskaya, N., Mangone, G., Biondetti, E., Valabrègue, R., Ewencyk, C., Hutchison, R.M., Cedarbaum, J.M., Corvol, J., Vidailhet, M., Lehericy, S., 2021. Longitudinal changes in neuromelanin MRI signal in Parkinson's disease: a progression marker. *Movement Disord* 36, 1592–1602. doi:10.1002/mds.28531.
- Graham, S.J., Henkelman, R.M., 1997. Understanding pulsed magnetization transfer. *J. Magn. Reson. Imaging* 7, 903–912. doi:10.1002/jmri.1880070520.
- Greenfield, J.G., Bosanquet, F.D., 1953. The brain-stem lesions in parkinsonism. *J. Neurol. Neurosurg. Psychiatry* 16, 213–226. doi:10.1136/jnnp.16.4.213.
- Halliday, G.M., Leverenz, J.B., Schneider, J.S., Adler, C.H., 2014. The neurobiological basis of cognitive impairment in Parkinson's disease. *Mov. Disord.* 29, 634–650. doi:10.1002/mds.25857.
- Huddleston, D.E., Langley, J., Dusek, P., He, N., Faraco, C.C., Crosson, B., Factor, S., Hu, X.P., 2018. Imaging Parkinsonian pathology in substantia nigra with MRI. *Curr. Radiol. Rep.* 6, 1–13. doi:10.1007/s40134-018-0272-x.
- Huddleston, D.E., Langley, J., Sedlaczik, J., Boelmans, K., Factor, S.A., Hu, X.P., 2017. *In vivo* detection of lateral-ventral tier nigral degeneration in Parkinson's disease. *Hum. Brain Mapp.* 38, 2627–2634. doi:10.1002/hbm.23547.
- Jenkinson, M., Beckmann, C.F., Behrens, T.E.J., Woolrich, M.W., Smith, S.M., 2012. FSL. *Neuroimage* 62, 782–790. doi:10.1016/j.neuroimage.2011.09.015.
- Ji, S., Choi, E.J., Kim, E.Y., Shin, D.H., Shin, H.G., Lee, J., 2021. High neuromelanin contrast achieved using sandwiched flow saturation RF pulses: sandwich-fsNM imaging. In: *Proceedings of the Annual Meeting, International Society for Magnetic Resonance in Medicine*, p. 1253 Presented at the International Society for Magnetic Resonance in Medicine.
- Kang, J., Kim, H., Kim, Eunjin, Kim, Eunbi, Lee, H., Shin, N., Nam, Y., 2021. Convolutional neural network-based automatic segmentation of substantia nigra on nigrosome and neuromelanin sensitive MR images. *Investig. Magn. Reson. Imaging* 25, 156–163. doi:10.13104/imri.2021.25.3.156.
- Kastner, A., Hirsch, E.C., Lejeune, O., Javoy-Agid, F., Rascol, O., Agid, Y., 1992. Is the vulnerability of neurons in the substantia nigra of patients with Parkinson's disease related to their neuromelanin content? *J. Neurochem.* 59, 1080–1089. doi:10.1111/j.1471-4159.1992.tb08350.x.
- Kim, E.Y., Sung, Y.H., Lee, J., 2019. Nigrosome 1 imaging: technical considerations and clinical applications. *Br. J. Radiol.* 92, 20180842. doi:10.1259/bjr.20180842.
- Langley, J., Huddleston, D.E., Liu, C.J., Hu, X., 2017. Reproducibility of locus coeruleus and substantia nigra imaging with neuromelanin sensitive MRI. *Magn. Reson. Mater. Phys. Biol. Med.* 30, 121–125. doi:10.1007/s10334-016-0590-z.
- Leutritz, T., Seif, M., Helms, G., Samson, R.S., Curt, A., Freund, P., Weiskopf, N., 2020. Multiparameter mapping of relaxation (R1, R2*), proton density and magnetization transfer saturation at 3 T: A multicenter dual-vendor reproducibility and repeatability study. *Hum. Brain Mapp.* 41, 4232–4247. doi:10.1002/hbm.25122.
- Liu, Y., Li, J., He, N., Chen, Y., Jin, Z., Yan, F., Haacke, E.M., 2020. Optimizing neuromelanin contrast in the substantia nigra and locus coeruleus using a magnetization transfer contrast prepared 3D gradient recalled echo sequence. *Neuroimage* 218, 116935. doi:10.1016/j.neuroimage.2020.116935.

- Matsuura, K., Maeda, M., Yata, K., Ichiba, Y., Yamaguchi, T., Kanamaru, K., Tomimoto, H., 2013. Neuromelanin magnetic resonance imaging in Parkinson's disease and multiple system atrophy. *Eur. Neurol.* 70, 70–77. doi:10.1159/000350291.
- Miyoshi, F., Ogawa, T., Kitao, S.I., Kitayama, M., Shinohara, Y., Takasugi, M., Fujii, S., Kaminou, T., 2013. Evaluation of Parkinson disease and Alzheimer disease with the use of neuromelanin MR imaging and 123I-metaiodobenzylguanidine scintigraphy. *Am. J. Neuroradiol.* 34, 2113–2118. doi:10.3174/ajnr.a3567.
- Moon, W.J., Park, J.Y., Yun, W.S., Jeon, J.Y., Moon, Y.S., Kim, H., Kwak, K.C., Lee, J.M., Han, S.H., 2016. A comparison of substantia nigra T1 hyperintensity in Parkinson's disease dementia, Alzheimer's disease and age-matched controls: volumetric analysis of neuromelanin imaging. *Korean J. Radiol.* 17, 633–640. doi:10.3348/kjr.2016.17.5.633.
- Morrison, C., Henkelman, R.M., 1995. A model for magnetization transfer in tissues. *Magn. Reson. Med.* 33, 475–482. doi:10.1002/mrm.1910330404.
- Nam, Y., Gho, S., Kim, D., Kim, E.Y., Lee, J., 2017. Imaging of nigrosome 1 in substantia nigra at 3T using multiecho susceptibility map-weighted imaging (SMWI). *J. Magn. Reson. Imaging* 46, 528–536. doi:10.1002/jmri.25553.
- Ohtsuka, C., Sasaki, M., Konno, K., Koide, M., Kato, K., Takahashi, J., Takahashi, S., Kudo, K., Yamashita, F., Terayama, Y., 2013. Changes in substantia nigra and locus coeruleus in patients with early-stage Parkinson's disease using neuromelanin-sensitive MR imaging. *Neurosci. Lett.* 541, 93–98. doi:10.1016/j.neulet.2013.02.012.
- Oshima, S., Fushimi, Y., Okada, T., Nakajima, S., Yokota, Y., Shima, A., Grinstead, J., Ahn, S., Sawamoto, N., Takahashi, R., Nakamoto, Y., 2020. Neuromelanin-sensitive magnetic resonance imaging using DANTE pulse. *Mov. Disord.* doi:10.1002/mds.28417.
- Pauli, W.M., Nili, A.N., Tyszka, J.M., 2018. A high-resolution probabilistic *in vivo* atlas of human subcortical brain nuclei. *Sci. Data* 5, 180063. doi:10.1038/sdata.2018.63.
- Pyatigorskaya, N., Gaurav, R., Arnaldi, D., Leu-Semenescu, S., Yahia-Cherif, L., Valabregue, R., Vidailhet, M., Arnulf, I., Lehericy, S., 2017. Magnetic resonance imaging biomarkers to assess substantia nigra damage in idiopathic rapid eye movement sleep behavior disorder. *Sleep* 40, zsx149. doi:10.1093/sleep/zsx149.
- Pyatigorskaya, N., Magnin, B., Mongin, M., Yahia-Cherif, L., Valabregue, R., Arnaldi, D., Ewencyk, C., Poupon, C., Vidailhet, M., Lehericy, S., 2018. Comparative Study of MRI Biomarkers in the Substantia Nigra to Discriminate Idiopathic Parkinson Disease. *Am. J. Neuroradiol.* 39, 1460–1467. doi:10.3174/ajnr.a5702.
- Pyatigorskaya, N., Yahia-Cherif, L., Gaurav, R., Ewencyk, C., Gallea, C., Valabregue, R., Gargouri, F., Magnin, B., Degos, B., Roze, E., Bardinet, E., Poupon, C., Arnulf, I., Vidailhet, M., Lehericy, S., 2020. Multimodal magnetic resonance imaging quantification of brain changes in progressive supranuclear palsy. *Mov. Disord.* 35, 161–170. doi:10.1002/mds.27877.
- Reimão, S., Lobo, P.P., Neutel, D., Guedes, L.C., Coelho, M., Rosa, M.M., Ferreira, J., Abreu, D., Gonçalves, N., Morgado, C., Nunes, R.G., Campos, J., Ferreira, J.J., 2015. Substantia nigra neuromelanin magnetic resonance imaging in de novo Parkinson's disease patients. *Eur. J. Neurol.* 22, 540–546. doi:10.1111/ene.12613.
- Sasaki, M., Shibata, E., Tohyama, K., Takahashi, J., Otsuka, K., Tsuchiya, K., Takahashi, S., Ehara, S., Terayama, Y., Sakai, A., 2006. Neuromelanin magnetic resonance imaging of locus ceruleus and substantia nigra in Parkinson's disease. *Neuroreport* 17, 1215–1218. doi:10.1097/01.wnr.0000227984.84927.a7.
- Schwarz, S.T., Rittman, T., Gontu, V., Morgan, P.S., Bajaj, N., Auer, D.P., 2011. T1-weighted MRI shows stage-dependent substantia nigra signal loss in Parkinson's disease. *Mov. Disord.* 26, 1633–1638. doi:10.1002/mds.23722.
- Schwarz, S.T., Xing, Y., Tomar, P., Bajaj, N., Auer, D.P., 2017. *In vivo* assessment of brainstem depigmentation in Parkinson disease: potential as a severity marker for multicenter studies. *Radiology* 283, 789–798. doi:10.1148/radiol.2016160662.
- Shibata, E., Sasaki, M., Tohyama, K., Otsuka, K., Endoh, J., Terayama, Y., Sakai, A., 2008. Use of neuromelanin-sensitive MRI to distinguish schizophrenic and depressive patients and healthy individuals based on signal alterations in the substantia nigra and locus ceruleus. *Biol. Psychiatry* 64, 401–406. doi:10.1016/j.biopsych.2008.03.021.
- Sulzer, D., Cassidy, C., Horga, G., Kang, U.J., Fahn, S., Casella, L., Pezzoli, G., Langley, J., Hu, X.P., Zucca, F.A., Isaias, I.U., Zecca, L., 2018. Neuromelanin detection by magnetic resonance imaging (MRI) and its promise as a biomarker for Parkinson's disease. *npj Park. Dis.* 4, 1–13. doi:10.1038/s41531-018-0047-3.
- Tessema, A.W., Lee, H., Gong, Y., Cho, Hwapyeong, Adem, H.M., Lyu, I., Lee, J., Cho, H.J., 2022. Automated volumetric determination of high R2* regions in substantia nigra: A feasibility study of quantifying substantia nigra atrophy in progressive supranuclear palsy. *NMR Biomed.* 35, e4795. doi:10.1002/nbm.4795.
- Trujillo, P., Petersen, K.J., Cronin, M.J., Lin, Y.C., Kang, H., Donahue, M.J., Smith, S.A., Claassen, D.O., 2019. Quantitative magnetization transfer imaging of the human locus coeruleus. *Neuroimage* 200, 191–198. doi:10.1016/j.neuroimage.2019.06.049.
- Trujillo, P., Summers, P.E., Ferrari, E., Zucca, F.A., Sturini, M., Mainardi, L.T., Cerutti, S., Smith, A.K., Smith, S.A., Zecca, L., Costa, A., 2017. Contrast mechanisms associated with neuromelanin-MRI. *Magn. Reson. Med.* 78, 1790–1800. doi:10.1002/mrm.26584.
- Wengler, K., He, X., Abi-Dargham, A., Horga, G., 2020. Reproducibility assessment of neuromelanin-sensitive magnetic resonance imaging protocols for region-of-interest and voxelwise analyses. *Neuroimage* 208, 116457. doi:10.1016/j.neuroimage.2019.116457.
- Xing, Y., Sapuan, A., Dineen, R.A., Auer, D.P., 2018. Life span pigmentation changes of the substantia nigra detected by neuromelanin-sensitive MRI. *Mov. Disord.* 33, 1792–1799. doi:10.1002/mds.27502.
- Xing, Y., Sapuan, A.H., Martín-Bastida, A., Naidu, S., Tench, C., Evans, J., Sare, G., Schwarz, S.T., Al-bachari, S., Parkes, L.M., Kanavou, S., Raw, J., Silverdale, M., Bajaj, N., Pavese, N., Burn, D., Piccini, P., Grosset, D.G., Auer, D.P., 2022. Neuromelanin-MRI to quantify and track nigral depigmentation in Parkinson's disease: a multicenter longitudinal study using template-based standardized analysis. *Mov. Disord.* 37, 1028–1039. doi:10.1002/mds.28934.
- Zecca, L., Stroppolo, A., Gatti, A., Tampellini, D., Toscani, M., Gallorini, M., Giaveri, G., Arosio, P., Santambrogio, P., Fariello, R.G., Karatekin, E., Kleinman, M.H., Turro, N., Hornykiewicz, O., Zucca, F.A., 2004. The role of iron and copper molecules in the neuronal vulnerability of locus coeruleus and substantia nigra during aging. *Proc. Natl. Acad. Sci. USA* 101, 9843–9848. doi:10.1073/pnas.0403495101.